catalysts

MDPI

Article

Aqueous Phase Reforming by Platinum Catalysts: Effect of Particle Size and Carbon Support

Xuan Trung Nguyen [1], Ella Kitching [2], Thomas Slater [2], Emanuela Pitzalis [1], Jonathan Filippi [3], Werner Oberhauser [3] and Claudio Evangelisti [1,*]

[1] Institute of Chemistry of OrganoMetallic Compounds (ICCOM), National Research Council (CNR), Via G. Moruzzi 1, 56124 Pisa, Italy; trung.nguyen@pi.iccom.cnr.it (X.T.N.); emanuela.pitzalis@cnr.it (E.P.)
[2] Cardiff Catalysis Institute (CCI), Cardiff University, Maindy Road, Cardiff CF24 4HQ, UK; kitchingea@cardiff.ac.uk (E.K.); slatert2@cardiff.ac.uk (T.S.)
[3] Institute of Chemistry of OrganoMetallic Compounds (ICCOM), National Research Council (CNR), Via Madonna del Piano 10, 50019 Sesto Fiorentino, Italy; jonathan.filippi@iccom.cnr.it (J.F.); werner.oberhauser@cnr.it (W.O.)
* Correspondence: claudio.evangelisti@cnr.it

Abstract: Aqueous phase reforming (APR) is a promising method for producing hydrogen from biomass-derived feedstocks. In this study, carbon-supported Pt catalysts containing particles of different sizes (below 3 nm) were deposited on different commercially available carbons (i.e., Vulcan XC72 and Ketjenblack EC-600JD) using the metal vapor synthesis approach, and their catalytic efficiency and stability were evaluated in the aqueous phase reforming of ethylene glycol, the simplest polyol containing both C–C and C–O bonds. High-surface-area carbon supports were found to stabilize Pt nanoparticles with a mean diameter of 1.5 nm, preventing metal sintering. In contrast, Pt single atoms and clusters (below 0.5 nm) were not stable under the reaction conditions, contributing minimally to catalytic activity and promoting particle growth. The most effective catalyst Pt_A/C^K, containing a mean Pt NP size of 1.5 nm and highly dispersed on Ketjenblack carbon, demonstrated high hydrogen site time yield (8.92 min^{-1} at 220 °C) and high stability under both high-temperature treatment conditions and over several recycling runs. The catalyst was also successfully applied to the APR of polyethylene terephthalate (PET), showing potential for hydrogen production from plastic waste.

Keywords: aqueous phase reforming; ethylene glycol; Pt catalyst; hydrogen production; nanoparticles; PET

Citation: Nguyen, X.T.; Kitching, E.; Slater, T.; Pitzalis, E.; Filippi, J.; Oberhauser, W.; Evangelisti, C. Aqueous Phase Reforming by Platinum Catalysts: Effect of Particle Size and Carbon Support. *Catalysts* **2024**, *14*, 798. https://doi.org/10.3390/catal14110798

Academic Editors: Georgios Bampos, Paraskevi Panagiotopoulou and Eleni A. Kyriakidou

Received: 10 October 2024
Revised: 25 October 2024
Accepted: 30 October 2024
Published: 7 November 2024

1. Introduction

In the search for sustainable energy solutions, renewable hydrogen (H_2) production has emerged as an important element in transitioning toward a low-carbon energy system. Traditionally, H_2 has been primarily produced from fossil fuels, such as natural gas, naphtha, or coal [1]. With the increasing environmental concerns related to non-renewable resource consumption, the focus has shifted toward exploring biomass as a H_2 production source, thanks to its CO_2 neutrality. Aqueous phase reforming (APR) has garnered significant attention as an effective method for converting biomass-derived feedstocks into hydrogen [2]. APR stands out due to its ability to process a wide range of organic sources, including mixed polyol streams, glycerol from biodiesel production, and waste streams from food industries and biorefineries [3]. These feedstocks can be valorized through APR to produce valuable hydrogen streams, thus addressing both waste management and energy production challenges. Furthermore, APR can be utilized as a solution to emerging waste problems; for example, increasing plastic waste is projected to reach 12 billion tons by 2050, demanding solutions for sustainability [4]. The valorization of plastic waste has attracted considerable interest as a sustainable alternative to traditional disposal methods. In addition to the widely explored

technologies, such as catalytic pyrolysis or steam reforming [5], APR remains relatively under-explored for hydrogen production from plastic waste.

The APR process is typically carried out at moderate temperatures, ranging from 220 to 265 °C, and pressures between 15 and 50 bar [6]. These conditions facilitate the conversion of alcohols and sugars into dihydrogen and carbon dioxide, thanks to the thermodynamically favorable water–gas shift reaction. The process's ability to operate at lower temperatures and higher pressures compared to conventional steam reforming eliminates the need to vaporize the feed stream, offering significant energy-saving advantages [7]. However, achieving high hydrogen selectivity in APR is challenging due to side reactions, such as methanation and dehydration/hydrogenation, which consume hydrogen to produce alkanes, alcohols, and organic acids [6,8].

Typically, APR is performed over heterogenous catalysts. Extensive research has identified supported metal catalysts, particularly those based on Pt, as highly effective for APR due to their high activity and selectivity toward hydrogen production [9,10]. The nature of the catalyst, including the active sites, support materials, and their interactions, significantly influences the product distribution and overall efficiency of the process.

The particle size of the NPs plays a critical role in the catalytic performance of the catalyst, as it affects the number of exposed active sites and also their electronic configuration [11]. Previous studies have reported the effect of Pt particle sizes in the aqueous phase reforming process [8]. However, different conclusions were drawn from the literature. The earliest result reported by Lehnert and Claus indicated that larger particles improved H_2 selectivity thanks to the abundance of terrace Pt sites [12]. The opposite conclusion was drawn by Wawrzet et al. when they studied glycerol APR with a Pt/Al_2O_3 catalyst [13]. They found that large particles slightly improved the conversion but reduced H_2 selectivity. Later, additional reports on the particle size effect on APR supported the result of Wawrzet et al. [14–17]. Generally, it is believed that smaller Pt particles (of approximately 1.5 nm) improve H_2 productivity. It must be noted that the particle sizes in the mentioned studies ranged from 1.1 nm upwards, while, to the best of our knowledge, no study has pointed out the role of sub-nano-Pt clusters in this reaction. Single-atom and cluster sites behave particularly differently from nanoparticles (NPs), prompting us to investigate this matter for the optimization of Pt catalysts [18,19].

In addition to the active metal, the support also plays an important role, particularly in catalyst activity and stability [20,21]. Compared to the commonly studied Al_2O_3 and SiO_2, which often suffer from low durability under APR conditions, carbonaceous supports have shown to be effective and stable for APR [22,23]. Moreover, the textural, morphological, and chemical properties of carbonaceous materials can be tuned widely to accommodate the objective. The interaction of the carbon support and the active metal can significantly influence catalyst performance. Therefore, the investigation of the effect of support on catalyst activity and stability is desirable to develop efficient catalysts for APR.

Metal vapor synthesis (MVS) is an advanced method that enables the formation of ultra-small NPs that can be immobilized on different supports without significant changes in particle size distribution [24]. This approach is particularly advantageous to decouple the effect of the particle size and role of support, in addition to its ability to generate an effective highly dispersed supported catalyst. In this work, we report for the first time the use of the MVS approach to make efficient Pt catalysts for APR of ethylene glycol (EG) as a model substrate. This substrate was chosen as it is the smallest polyol containing both C-O and C-C bonds. The simplicity of EG allows for easier assessment of the catalyst's activity, while still incorporating the key chemical structure found in the target substrates used in APR, such as polyols and carbohydrates. The effects of support and particle sizes (in a range less than 2 nm) were also investigated. Furthermore, the best-performing catalysts were used in the application of APR using polyethylene terephthalate (PET) as a substrate to make H_2, exhibiting the feasibility of the catalyst in providing an alternative for waste plastic valorization.

2. Results and Discussion

2.1. Synthesis and Characterization of Carbon-Supported Pt Catalysts

Pt-based catalysts were synthesized by the MVS method, as depicted in Scheme 1 [25]. This approach guarantees the formation of heterogeneous catalysts containing small Pt NPs (<5 nm), with narrow size distribution, in their reduced form without residues (such as halides derived from metal salt precursors, or stabilizing agents). Moreover, the metal NPs' size can be controlled by exploiting the coordinative properties of the solvent used. In particular, we recently reported that carbon-supported Pt catalysts with a very high metal dispersion and sub-nano-Pt clusters, regardless of the support employed, were obtained by the co-condensation of Pt atoms and mesitylene solvent vapor [26]. Unlike mesitylene, the less-coordinating property of acetone was exploited to prepare Pt-NPs of slightly larger sizes [27]. As supports, we selected two commercially available carbonaceous supports, largely used for (electro)catalytic applications: Vulcan XC72 (C^V) and Ketjenblack EC-600JD (C^K) (see Table S1 for their textural and structural properties). The simple addition of MVS-derived acetone or mesitylene-solvated Pt nanoclusters (Pt_A and Pt_M, respectively) to the desired support (i.e., C^V or C^K) gave the corresponding heterogeneous supported catalysts Pt_A/C^V, Pt_AC^K, and Pt_M/C^K as in Scheme 1. Additionally, each catalyst was subjected to heat treatment at 500 °C under an inert atmosphere for 2 h, to evaluate the stability and possible restructuring of the Pt NPs under these conditions. As a result, six different Pt-based catalysts were obtained, all samples containing a Pt loading of 2.0 wt.%, as confirmed by ICP-OES.

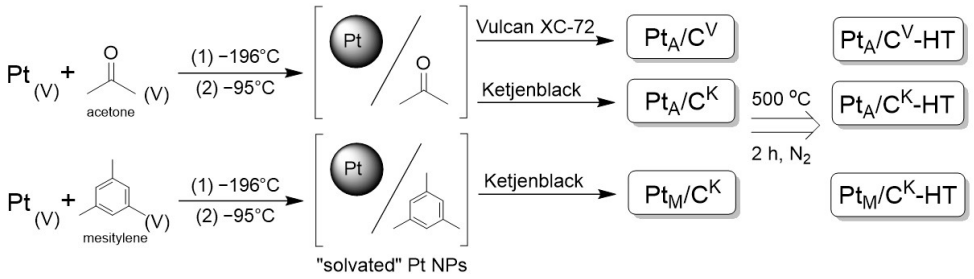

Scheme 1. Schematic synthesis of Pt-based catalysts supported on carbon by MVS method.

An HRTEM analysis of both the freshly prepared catalysts derived from Pt–acetone nanoclusters (i.e., Pt_A/C^K and Pt_A/C^V) showed the presence of Pt-NPs having a mean diameter of 1.5 nm (standard deviation, SD = 0.3 nm), highly dispersed onto the carbon supports (Figure 1). On the other hand, the Pt_M/C^K sample obtained from Pt–mesitylene nanoclusters (Figure S1, Supplementary Information) exhibited, as expected, Pt NPs < 1.5 nm in size, suggesting the presence of sub-nano-atoms/clusters that were not detected by a conventional TEM analysis.

In order to gain further information about the structure of the catalysts, high-angle annular dark field (HAADF) imaging with an aberration-corrected scanning transmission electron microscope (STEM) was conducted. To obtain deeper information about the structure of the catalysts in the sub-nanometer range, HAADF imaging with aberration-corrected STEM was carried out on both Pt–acetone- and Pt–mesitylene-derived catalysts dispersed on C^K carbon. The analysis revealed a strong difference between the two samples that showed a completely diverse arrangement of the Pt atoms in the sub-nanometer range (Figure 2). Indeed, the Pt_M/C^K catalyst showed a relatively high proportion of single atoms (6.2 at.%) and clusters below 1 nm (mean diameter of 0.4 nm, single atoms excluded from calculation) (Figure 2, right side). On the other hand, in the analogous samples prepared from Pt–acetone, no Pt single atoms or small clusters (<0.2 at.%) were observed, but only well-formed NPs centered at 1.5 nm (Figure 2, left side), confirming the above discussed particle size distribution obtained by conventional TEM. An analysis of the Fourier transforms of atomic resolution HAADF-STEM images was conducted to identify

crystallographic directions of the nanoparticle facets in samples Pt_M/C^K and Pt_A/C^K. Where NPs formed in the Pt_M/C^K sample, the majority lacked distinct facets, and instead appeared to be amorphous, with structures ranging from circular and ovoid to chain-like branches of atoms. In Pt_A/C^K samples, the majority of the NPs that formed appeared to be circular, amorphous, and therefore non-faceted. However, in the 1.0–1.5 nm diameter range, a minority of FCC NPs with {111} facets were observed.

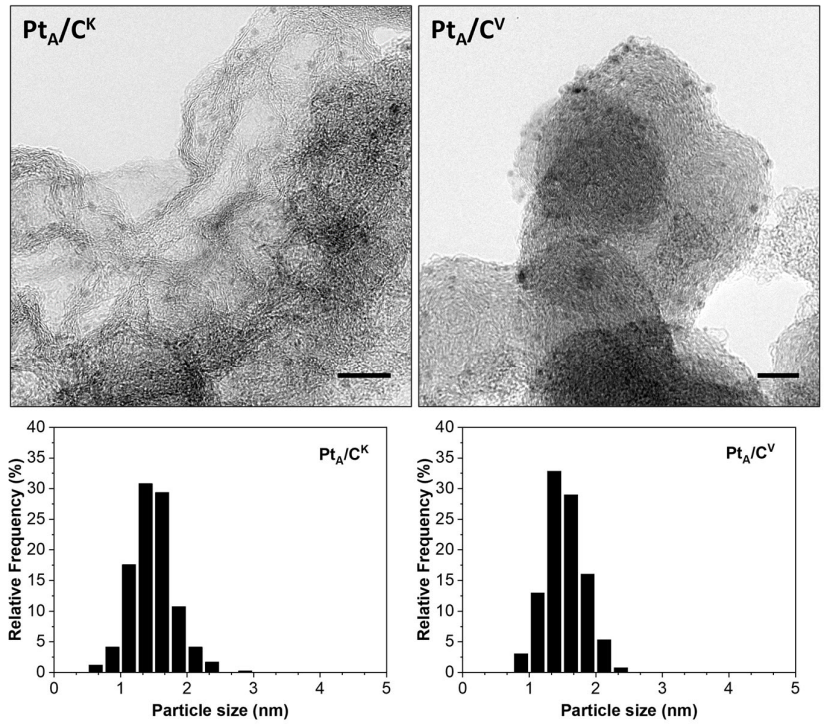

Figure 1. Representative TEM images at high magnification (the bar in the images corresponds to 10 nm) and particle size distributions of Pt_A/C^K (**left side**) and Pt_A/C^V (**right side**).

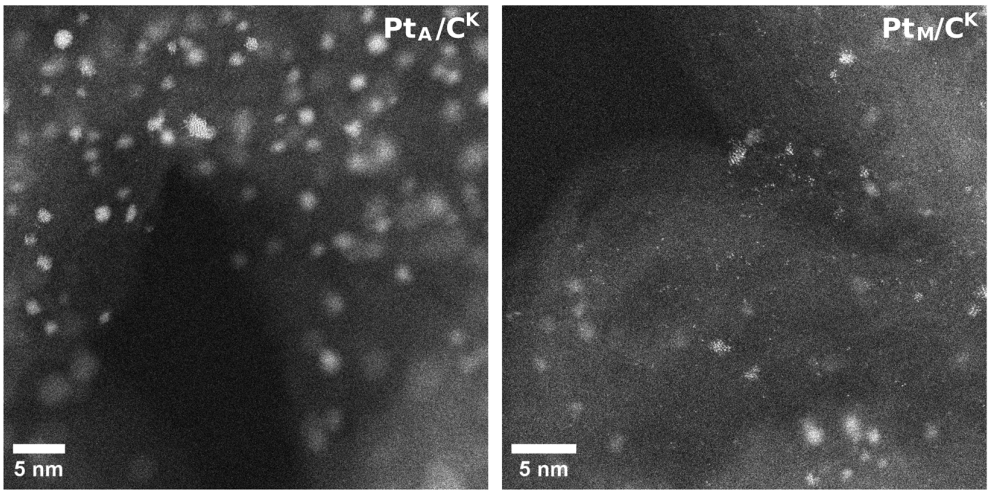

Figure 2. Representative HAADF STEM images of Pt_A/C^K (**left side**) and Pt_M/C^K (**right side**).

The TEM analysis of the heat-treated samples (500 °C, 2 h) demonstrated the crucial role of both the starting NP sizes and the support on the stability of the catalyst against the sintering of the Pt active phase. Interestingly, the best result in terms of stability was observed with the Pt_A/C^K system, where the Pt NPs retained the initial sizes

after thermal treatment (d_m = 1.5 nm; SD = 0.3) (Figure 3, left side). The Pt–acetone-derived sample supported on Vulcan carbon showed a slight increase in the NP sizes (d_m = 1.6 nm; SD = 0.6 nm) (Figure 3, right side), demonstrating the high thermal stability of the acetone-derived NPs towards the metal sintering, regardless of the carbon support (i.e., C^K or C^V) used. On the other hand, the mesitylene-derived samples revealed a lower thermal stability. Indeed, for the Pt_M/C^K-HT, a significant increase over the mean NP size (3.6 nm; SD = 7.6) was observed (Figure S2, Supplementary Information). Pt_M/C^K-HT NPs typically fell into one of two size categories, a 1–3 nm diameter or greater than a 10 nm diameter, resulting in a high standard deviation of particle size. While some of the smaller NPs in the 1–3 nm diameter range remained amorphous, the majority crystallized into FCC structures, alongside the larger NPs. These crystalline FCC NPs displayed both {110} and {111} facets, with the {111} facets observed approximately three times more frequently than the {110} facets.

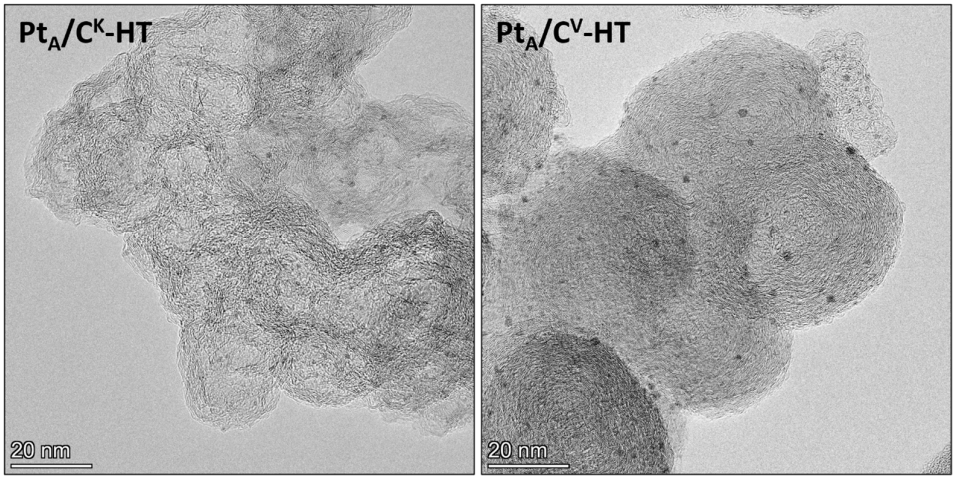

Figure 3. Representative TEM images of Pt_A/C^K-HT (**left side**) and Pt_A/C^V-HT (**right side**).

The mean particle diameters observed for the different carbon-supported Pt catalysts are summarized in Table 1, together with the corresponding Pt dispersions determined by estimating the total surface atoms and bulk atoms in each observed NP [28]. As a result, the freshly prepared Pt–acetone-derived catalysts (i.e., Pt_A/C^K and Pt_A/C^V) give, as expected, very similar metal dispersions of 63% and 62%, respectively (entries 1 and 2, Table 1), whereas the Pt–mesitylene-derived catalyst (entry 3) exhibited a higher dispersion (73%). The results acquired on the heat-treated catalysts revealed a high stability of the NPs in the Pt–acetone-derived samples, which contrasts with the Pt_M/C^K, where due to the NP aggregation, an inhomogeneous size distribution was registered; hence, the estimation of the Pt dispersion based on TEM measurements was not reliable.

Table 1. Characterization of MVS-derived carbon-supported Pt catalysts.

Entry	Catalyst [(a)]	Mean Pt NP Diameter/Standard Deviation	Dispersion (Calculated)
1	Pt_A/C^K	1.5/0.31 nm	63%
2	Pt_A/C^V	1.5/0.34 nm	62%
3	Pt_M/C^K	0.35/0.35 nm [(b)]	73% [(c)]
4	Pt_A/C^K-HT	1.5/0.29 nm	63%
5	Pt_A/C^V-HT	1.6/0.54 nm	50%
6	Pt_M/C^K-HT	3.3/7.38 nm	n.d. [(d)]

[(a)] The Pt loading was fixed to 2.0 wt.% for all the catalysts; [(b)] single-site atoms included; [(c)] single-site atoms not included; [(d)] not determined.

The reported results above reveal that the solvent used for NP synthesis by the MVS method plays a crucial role not only in the final Pt NPs' size, but also in the thermal stability of the particles against the sintering process. In the MVS procedure, when the Pt–solvent solid matrix is warmed, metal cluster/particle nucleation takes place and the interaction between the metal atoms and the solvent drives the formation of the final NPs [29]. As discussed above, the interaction of acetone with Pt atoms led to the formation of NPs with a size distribution centered on a diameter of 1.5 nm, with a high stability against sintering at a high temperature. This mean diameter was previously reported to correspond to the formation of metastable Pt NPs containing 147 Pt atoms in both cuboctahedral and icosahedral geometries by DFT [30]. On the other hand, the single atoms and the very small clusters observed in the Pt_M/C^K had the tendency to form larger NPs after heat treatment, suggesting a lower stability to elevated temperature (see Table 1) [31,32].

To further characterize the surface properties of Pt nanoparticles (NPs) in the MVS-derived Pt catalysts, CO-stripping experiments, known for their high sensitivity and reliability for the determination of the surface area of Pt NP surfaces, were conducted [33–35]. The oxidation potential, at which the reaction between surface-adsorbed CO and OH^- groups occurs via a Langmuir–Hinshelwood mechanism, is significantly influenced by the size, morphology, and degree of agglomeration of the NPs. The CV profiles of each catalyst resemble the typical features of platinum (Figure S3, Supplementary Information), with hydrogen adsorption/desorption peaks in the 0–0.1 V vs. RHE range, surface Pt-OH formation around 0.6 V vs. RHE, and the platinum surface oxidation wave at potentials higher than 1 V, followed by the Pt-O reduction in the reverse scan around 0.6 V. The samples using C^K as support show higher differential background capacitance due to the higher surface area of the support itself. CO-stripping experiments (Figure 4) show onset, peak potential, and measured electrochemical accessible surface area (EASA) that are very close for acetone–Pt samples, suggesting that the nature of platinum in each sample is similar. An increase in EASA when heating Pt_A/C^K at 500 °C for 2 h was observed, suggesting that the heat treatment is effective to remove acetone from the micropores of the carbon support, leading to an increase in the exposed metal surface. On the contrary, a shift to a lower onset and high EASA reported on Pt_M/C^K aligned well with the presence of the smallest Pt NPs, Pt clusters, and atoms recorded by the TEM analysis. Additionally, heat treatment of Pt_M/C^K negatively impacted EASA, a reduction of about 60% (Figure 4B). Pt_M/C^K-HT also exhibited a broad and poorly defined J/E curve, consistent with the presence of NPs having a wide size distribution, confirming that a noticeable sintering phenomenon occurred during the heat treatment, as observed with the TEM analysis.

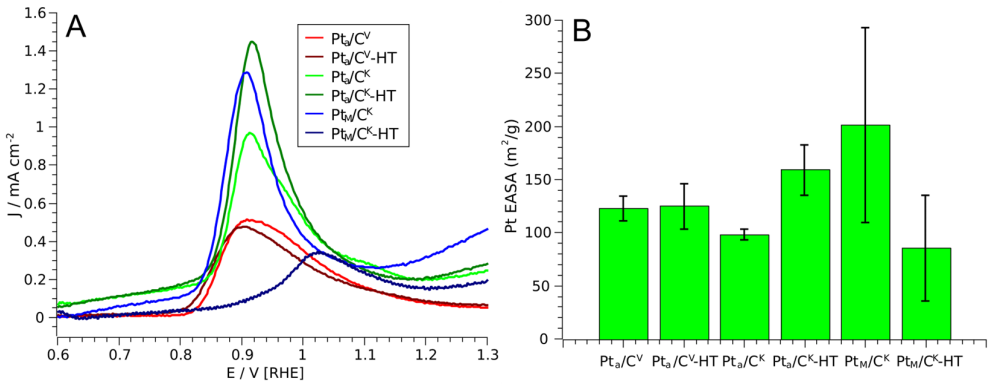

Figure 4. CO-stripping voltammetry (baseline-corrected) of the MVS-derived Pt/C catalysts (**A**); CO stripping-derived Platinum Electrochemical Accessible Surface Area (EASA) of the MVS-derived Pt/C catalysts with error bars (standard deviation) (**B**).

2.2. Catalytic Performance of MVS-Derived Supported Pt Catalysts

2.2.1. Aqueous Phase Reforming of Ethylene Glycol

Ethylene glycol (EG) was selected as a model compound to evaluate the catalytic performance of the carbon-supported Pt catalysts in the APR process. EG is an attractive platform molecule, not only due to its potential as a secondary raw material sourced from biomass, sugars, and alcohols [9], but also because it is the simplest polyol containing both C-C and C-O bonds. Thus, EG reforming can serve as a model process for the direct production of hydrogen from biomass-derived sugars, such as glucose, and sugar alcohols like sorbitol.

The mechanism of hydrogen production from EG was previously extensively investigated by Dumesic et al. [36] and is summarized in Scheme 2. The formation of H_2 and CO_2 takes place by means of C-C and C-O bond cleavage and a further water gas shift reaction (WGS). Meanwhile, side reactions leading to liquid products mainly include (a) dehydration followed by hydrogenation to form ethanol and methanol by further hydrogenolysis; (b) dehydrogenation producing acetic acid. Finally, methane and high-carbon alkanes can be formed via Fischer–Tropsch and methanation reactions in the gas phase.

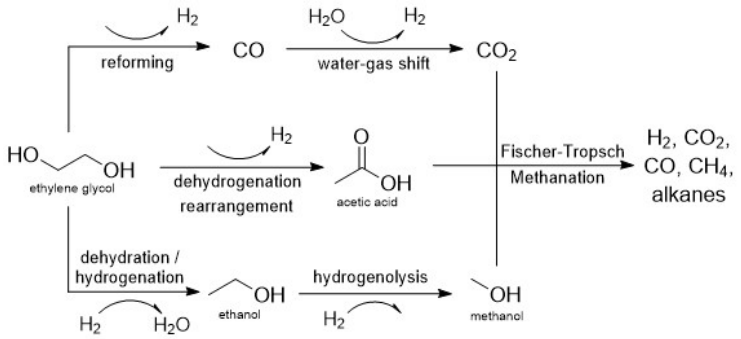

Scheme 2. Reaction pathway of APR of ethylene glycol.

The catalytic results obtained with the Pt-based catalysts are reported in Figure 5 and in Table 2. The turnover frequency (TOF) of the catalyst was calculated as the moles of ethylene glycol (EG) converted per minute per exposed Pt atom, using the measured dispersion. Likewise, the hydrogen site time yield (H_2 STY) was determined as the amount of hydrogen produced per minute per exposed Pt atom. The reactions were performed in mild conditions (T = 220 °C for 4 h) compared to conventional APR conditions in order to properly compare and point out the catalytic properties of the different Pt catalysts.

Generally, a negligible amount of CO, CH_4, and other higher alkanes were found in the gas phase of all catalytic runs. This is expected as Pt-based catalysts are not strong methanation catalysts, while a low temperature favors the WGS, minimizing the formation of CO. Very high selectivity (ranging from 81% to 90%) towards gaseous products (i.e., H_2 and CO_2) was observed for all the catalysts, along with a small amount of liquid products, primarily ethanol and methanol (Figure 5B). No formation of acetic acid was observed. It has been reported that acetic acid could be formed via a bifunctional route: dehydrogenation by the metal phase and rearrangement by an acidic support [36]. In our case, since the supports used (i.e., C^V and C^K) are slightly basic [37], it is likely that the rearrangement step was suppressed, resulting in a negligible amount of acetic acid formed. This is particularly beneficial as carboxylic acid products are commonly undesirable, offering low-value chemicals compared to the feed.

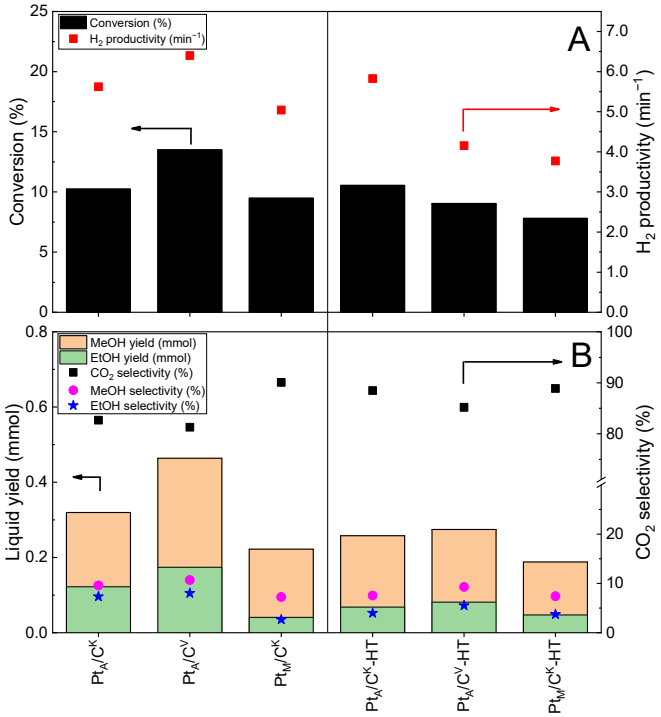

Figure 5. (**A**) EG conversion and hydrogen productivity of supported Pt catalysts. (**B**) Liquid yield and CO_2 selectivity of supported Pt catalysts. Reaction conditions: 220 °C, 4 h, 50 mg Pt/C (2.0 Pt wt.%, 5.1 µmol Pt), 20 mL H_2O, EG 5 wt.%.

Table 2. Numerical data of APR of EG by supported MVS-derived Pt catalysts [(a)].

Entry	Catalyst	EG Conv. (%)	H_2 Sel. (%)	TOF (min^{-1})	H_2 STY (min^{-1})
		Freshly prepared catalyst			
1	Pt_A/C^K	10.2%	83%	2.14 min^{-1}	8.92 min^{-1}
2	Pt_A/C^V	13.9%	77%	2.67 min^{-1}	10.32 min^{-1}
3	Pt_M/C^K	9.5%	81%	1.70 min^{-1}	6.91 min^{-1}
		Heat-treated catalysts (500 °C, 2 h, N_2)			
4	Pt_A/C^K—HT	10.5%	89%	2.06 min^{-1}	9.25 min^{-1}
5	Pt_A/C^V—HT	9.0%	79%	2.07 min^{-1}	8.31 min^{-1}
6	Pt_M/C^K—HT	7.8%	73%	n.d. [(b)]	n.d.

[(a)] Reaction conditions: T = 220 °C, t = 4 h, 50 mg Pt/C (2.0 Pt wt.%, 5.1 µmol Pt), 20 mL H_2O, EG 5 wt.%; [(b)] not determined.

The comparison among the freshly prepared Pt catalysts (left side of Figure 5 and entries 1–3 of Table 2) points out the crucial role of the initial size of the Pt active phase, which was controlled by the solvent used for the catalyst's synthesis (i.e., acetone or mesitylene), and the kind of carbon support (i.e., Vulcan or Ketjenblack) on the activity and stability of the catalyst. The stabilizing effect of the carbonaceous support was clearly observed in the results, particularly when acetone was used as the coordinating solvent. While freshly prepared Pt_A/C^V showed higher activity compared to Pt_A/C^K, it experienced significant deactivation after heat treatment, with about a 30% drop in both ethylene glycol conversion and hydrogen productivity. The TEM analysis revealed that heat treatment caused a larger NP size distribution in Pt_A/C^V (i.e., lower Pt dispersion, see Table 1), likely explaining its lower performance. In contrast, Pt_A/C^K demonstrated exceptional stability up to 500 °C with virtually no change in EG conversion (from 10.2% to 10.5%), H_2 productivity (from 5.62 min^{-1} to 5.83 min^{-1}), or liquid product distribution. This finding is supported by the unchanged morphology and size of Pt_A/C^K found by TEM characterization. When examining the dispersion of Pt NPs, the calculated

TOF and H_2 site time yield (STY) highlighted the effect of particle size. Pt_A/C^K and Pt_A/C^K-HT shared similar particle size distributions and showed comparable values (8.92 min^{-1} and 9.25 min^{-1}, respectively). The heat-treated Pt_A/C^V-HT, despite showing only a slight increase in particle size and distribution, suffered a significant drop in both TOF and H_2 STY (a reduction of nearly one-fifth in both values) compared to the pristine Pt_A/C^V. This considerable decrease in performance cannot be attributed solely to the loss of the Pt surface due to sintering. Instead, it aligns with previous studies that suggest that quantum effects become significant when NP sizes fall below 1.6 nm [13,15–17]. For example, Yamaguchi and Tai reported a 36% decrease in TOF when Pt particle size increased from 1.5 nm to 1.6 nm. The effect of particle size upon heat treatment was further corroborated by the case of Pt_A/C^K. Thus, the results showed that C^K provides greater stability for supported Pt NPs, particularly those containing NPs of 1.5 nm in size. The enhanced stability of the C^K-supported system could be attributed to a higher specific area and pore volume, which facilitates higher dispersion of Pt NPs [38,39]. Interestingly, hydrogen selectivity for both Pt_A/C^K and Pt_A/C^V slightly improved after heat treatment (from 83% to 89%, and from 77% to 79%, respectively). This could be due to increased particle crystallinity, as well-ordered Pt facets may facilitate C–C bond cleavage. Indeed, heat-treated samples showed higher crystallinity than that observed in the freshly prepared samples (vide supra). This improvement in crystallinity, and consequently in hydrogen selectivity, could also result from exposure to reaction conditions, as discussed in the recycling tests reported below.

Surprisingly, when mesitylene was used as the coordinating solvent, despite the abundance of sub-nanometer Pt sites (i.e., single atoms or clusters), much lower TOF and H_2 STY values were observed (entry 3, Table 2) with respect to the analogous system derived from acetone containing NPs. Moreover, it must be considered that for the calculation of the TOF of the Pt_M/C^K, the contribution of the single Pt atoms was excluded (see dispersion value reported in Table 1). These results suggest that the presence of sub-nanometer Pt atoms and clusters does not boost the catalytic efficiency of this process. This observation can be tentatively explained by the reaction mechanism of APR. Cleavage of C–C and C–O bonds occurs through the adsorption of reactants and intermediates on Pt surfaces. Density Functional Theory (DFT) calculations and microkinetic studies suggest that the most stable binding modes of these intermediates are bidentate or tridentate configurations, which require adjacent Pt atoms or Pt planes to facilitate dissociation reactions [9,40–42].

In contrast to Pt_A catalysts, upon heating to 500 °C, the mesitylene–Pt-based catalyst (i.e., Pt_M/C^K-HT) showed a significant drop in catalytic activity (a reduction of about 25% in both conversion and H_2 productivity) (Figure 5). This strong decrease in performance of the system likely reflects the severe sintering that occurred, as observed by the TEM analysis. Indeed, the high mobility of Pt single atoms and clusters onto the carbon support led to particle size growth in the heat-treated catalysts (see Table 1), which negatively impacted the catalyst's performance. Overall, acetone-derived Pt NPs dispersed on C^K support proved to be the most effective catalyst for the APR of EG, in terms of both activity and stability under heat treatment. Additionally, a comparison between commercial Pt/Al_2O_3 (Sigma-Aldrich, St. Louis, MO, USA) containing Pt NPs with a mean diameter of 4.7 nm (Figure S5), serving as a benchmark catalyst, showed a remarkable improvement in Pt_A/C^K in EG conversion and H_2 productivity (10.2% vs. 5.5% and 5.62 min^{-1} vs. 3.04 min^{-1}), demonstrating the superior efficiency of our MVS-derived catalyst (Figure S4).

2.2.2. Recycling Tests

Since Pt_A/C^K was the best-performing catalyst among those screened, we proceeded to investigate the stability of this catalyst with recycling tests. In the recycling test, a higher amount of catalyst was used to minimize the effect of material loss during recovery. The reaction was performed at 240 °C for 2 h under 7 bar N_2. After collecting the gas and liquid samples, we filtered and dried the catalyst, followed by running three more catalytic reactions under the same experimental conditions. The results are shown in Figure 6. It can be clearly seen that the catalyst possesses good stability with a slight decrease in EG conversion only after the first run (from 30.9% to 22.2%), then stabilizing in the consecutive runs. On the

contrary, the H_2 productivity did not experience any significant change (from 4.96 min^{-1} Pt to 4.82 min^{-1}). In the liquid phase, after the first run, where ethanol and methanol selectivity were high, the following runs showed consistent liquid composition. It is likely that the catalyst underwent restructuring in the first run to be stabilized by the reaction environment. In fact, the observed decrease in the yield of the liquid products along with an increased H_2 selectivity was similar to the heat treatment case. Afterwards, the catalyst performed consistently, indicating that it reached a stable configuration. The TEM analysis of the catalyst after four runs (Figure S6) shows only a slight increase in the mean NP size (dm = 1.7 nm). Moreover, the ICP-OES analysis of the used catalyst showed negligible leaching of Pt into the solution, confirming the stability of our catalyst. In conclusion, our Pt_A/C^K is a promising catalyst for APR thanks to its high stability and activity.

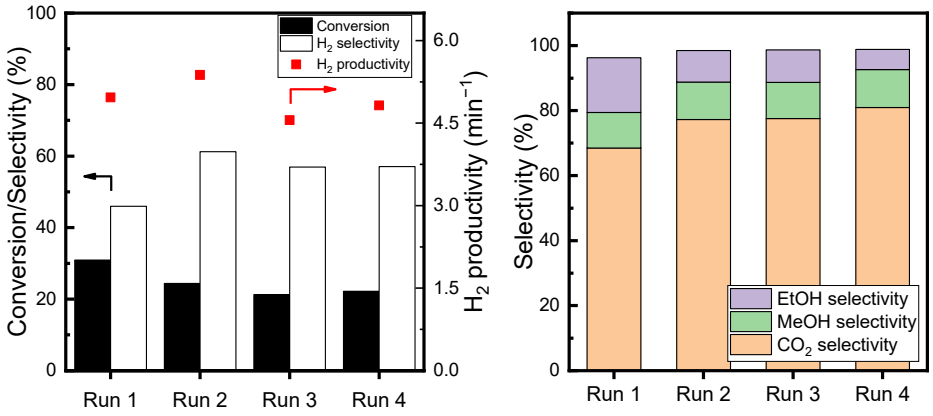

Figure 6. Recycling test of Pt_A/C^K in APR of EG. Reaction conditions: 240 °C, 2 h, 200 mg of catalyst (2.0 Pt wt.%, 20.5 µmol Pt), 20 mL H_2O, EG 5 wt.%.

2.2.3. Aqueous Phase Reforming of PET

In this study, we utilized the highest-performing MVS catalyst (Pt_A/C^K) to explore hydrogen generation through the APR of polyethylene terephthalate (PET), a primary plastic accounting for 8% by weight of solid waste worldwide [43]. Our data are shown in Table 3. A blank test shows that depolymerization reaches completion with 100% recovery of EG in 2 h at 240 °C under 7 bar N_2. From the results, H_2 productivity of Pt_A/C^K was found to be 1.14 min^{-1} (entry 1, Table 3). Increasing the reaction time and the amount of the catalyst resulted in lower productivity (entry 2, Table 3). This is likely due to a negative effect of the formation of products that slowed down the reaction rate. Indeed, the formation of gaseous products, resulting in an increase in pressure in the batch condition, was reported to have a negative effect on the APR reaction [8].

Table 3. Aqueous Phase Reforming of PET under neutral condition [(a)].

Entry	Catalyst	PET (g) /Metal (mol)	Time	EG Conv. (%)	H_2 Prod. (min^{-1})	Ref.
1	Pt_A/C^K	136,500	2 h	12.8%	1.14	This work
2	Pt_A/C^K	68,250	4 h	38.5%	0.87	This work
3 [(b)]	Pt_A/C^K	68,250	2 h	0%	0	This work
4 [(c)]	Pt/Al_2O_3 com	68,250	4 h	10.3%	0.13	This work
5	Ru/MEC	10,100	-	-	0.67	[44]
6	Ru/ZnO/MEC	10,100	-	-	1.26	[45]
7	Pt/ENS	4333	-	-	0.9	[5]

[(a)] Reaction conditions: 240 °C, Pt catalyst, 50 mL H_2O, 700 mg of crushed PET; [(b)] NaOH 4 wt.%; [(c)] commercial Pt/Al_2O_3 1 wt.%, purchased from Sigma-Aldrich (Milwaukee, WI, USA).

The productivity of the Pt_A/C^K for APR of PET was lower than that obtained in the APR process of EG, carried out in analogous reaction conditions (i.e., 4.96 min^{-1}, see Figure 5, Run 1). In addition to the fact that the depolymerization reaction happened quantitatively, it is likely that the presence of produced terephthalic acid (TPA) has a negative effect on APR of EG. We observed a similar phenomenon with the commercial Pt/Al_2O_3 catalyst, which exhibited much lower productivity in the APR of PET than in the case of pure EG (entry 4, Table 3 and Figure S4, Supplementary Information). This behavior is distinctively different from the Ru-based catalyst reported by Su et al., where TPA did not influence the activity of the catalyst [45]. Furthermore, the authors reported that basic conditions are beneficial for the process. On the other hand, in our case, the use of basic conditions showed a detrimental effect on the efficiency of the Pt-based catalyst (entry 3, Table 3). Increasing the pH of the solution resulted in negatively charged terephthalates, which might strongly coordinate to Pt atoms of the electron-deficient Pt surface, preventing the absorption of EG and thus deactivating the catalyst [46]. In fact, several studies have reported the inhibition effect of aromatic carboxylic acid on noble metal particle growth and stabilization [47,48].

Literature examples concerning the usage of heterogeneous catalysts for APR of PET plastic are still limited. In Table 3, we compared our catalyst's productivity with all reported studies on this subject to date. As all of the studies were performed at different conditions and reactor configurations, a direct comparison of the catalysts is challenging. Nevertheless, we chose H_2 productivity as a representative indicator as it could somewhat reflect the intrinsic catalytic activity of the materials. As shown, Pt_A/C^K was among the highest H_2 productivities among examined catalysts under neutral conditions. Our catalyst can perform efficiently without the assistance of a base (i.e., corrosiveness of the base is avoided), in contrast to Ru-based catalysts [44]. A further optimization of operating parameters for the best-performing Pt catalyst will be investigated in a forthcoming study.

3. Materials and Methods

3.1. Catalyst Synthesis

The Pt nanoparticles were generated by metal vapor synthesis (MVS), which was reported previously [26]. To prepare the supported Pt catalysts, platinum vapor was generated at 10^{-5} mbar by resistive heating of a tungsten wire coated with approximately 100 mg of electrodeposited platinum. This metal vapor was co-condensed with 100 mL of solvent (either acetone or mesitylene) vapor at −196 °C (liquid nitrogen) in the MVS reactor. The reactor was then warmed to the melting point of the solid matrix (−95 °C for Pt–acetone matrix and −40 °C for Pt–mesitylene), resulting in a dark brown solution (95 mL). This solvated Pt solution was siphoned at −40 °C into a Schlenk tube and stored at −20 °C. The ICP-OES analysis showed that the Pt solution contained approximately 0.5 mg/mL Pt. To obtain the supported catalysts, the solutions were added to the suspension of carbonaceous supports (Vulcan XC-72 and/or Ketjenblack EC600J) in the matching solvent. The mixtures were stirred at 25 °C for 20 h to ensure complete deposition. The solids were collected after washing three times with 50 mL of *n*-pentane each. Finally, the catalysts were dried under reduced pressure at room temperature.

For heat treatment of catalysts, a set amount of a catalyst (150 mg) was loaded into a ceramic boat and heated under N_2 flow (100 mL/min) in a tubular furnace to a designated temperature. The heating rate was 10 °C/min and the dwell time was 2 h at 500 °C. The heat-treated catalysts were labeled with "HT" (for heat-treated) as a suffix.

3.2. Catalyst Characterization

TEM imaging was performed using a Talos™ F200X G2 TEM (Thermo Scientific, Waltham, MA, USA). Samples for the analysis were prepared by their suspension in isopropyl alcohol and were ultrasonically dispersed followed by the deposition of a drop of the suspension on a holey carbon-coated copper grid (300 mesh). The histograms of the metal particle size distribution were obtained by counting at least 300 particles in

the micrographs. The mean particle diameter (d_m) was calculated by using the formula $d_m = \sum d_i n_i / \sum n_i$, where ni is the number of particles with diameter d_i. Metal dispersion was calculated based on the work of Borodziński et al. [28].

High-angle annular dark field (HAADF) STEM images were acquired on a JEOL ARM200F microscope and a JEOL ARM300F (JEOL, Tokyo, Japan) at the electron Physical Science Imaging Centre (ePSIC) at Diamond Light Source. The JEOL ARM200F was operated at an acceleration voltage of 200 kV, with a convergence semi-angle of 23 mrad and an inner collection angle of 79 mrad. The JEOL ARM300F was operated at an acceleration voltage of 300 kV, a convergence semi-angle of 26.2 mrad, a beam current of 25 pA, and an approximate inner collection angle of 92.6 mrad. Further HAADF-STEM images were acquired on a Thermo Fisher Spectra 200 (Thermo Fischer, Waltham, MA, USA) at Cardiff University, which was operated at an accelerating voltage of 200 kV, a beam current of 60 pA, and a convergence semi-angle of 29.5 mrad. The HAADF images were collected with an inner collection angle of 56 mrad, and an outer collection angle of 200 mrad. A 5–15 min beam shower was completed prior to imaging on all microscopes to reduce contamination. Samples for electron microscopy were prepared by their suspension in isopropyl alcohol and ultrasonic dispersion, followed by a deposition of a drop of the suspension onto a 300-mesh holey carbon-coated grid of either molybdenum, copper, or gold. The particle size distribution analysis was completed via the ParticleSpy Python package (reference to https://zenodo.org/records/5094360, accessed on 30 July 2023). Automated particle detection and measurement were performed using Otsu filtering, with the manual counting verification of single atoms to ensure accuracy.

ICP-OES analyses were carried out with an ICP-Optical emission dual-view Perkin Elmer OPTIMA 8000 apparatus (Perkin Elmer, Waltham, MA, USA). For analyzing the MVS solution, 0.5 mL of a Pt-SMA solution was heated over a heating plate in a porcelain crucible to remove the solvent, followed by dissolving the solid residue in 2 mL of aqua regia in 6 h. The solution was then diluted with 50 mL of HCl 0.5 M. For catalyst loading measurements, approximately 10 mg of a catalyst was dissolved in 4 mL of aqua regia and fluxed for 6 h. The solution was then diluted with 50 mL of HCl 0.5 M. The quantification of Pt was performed with calibration with Pt solutions of known concentrations. The limit of detection (l.o.d) calculated for platinum was 2 ppb. In all cases, the results of MVS solution and catalyst loading were highly consistent. A quantitative deposition of NPs onto the support was obtained, leading to a final 2.0 wt.% Pt loading for all the catalysts.

The CO-stripping analysis was performed as follows: each catalyst sample powder was dispersed (10 mg) in a mixture of 100 µL ultrapure water and 1 g 2-propanol by using an ultrasonic bath for 60 min. The homogeneous ink was then cast onto a glassy carbon disk (Pine™ Electrodes, A = 0.1963 cm^2) in two steps: 5 µL of ink was added in 2.5 µL steps using a 2–20 µL micro-pipette and dried after each step; the ink quantity was determined by weight before drying. After complete drying, 1.6 µL of 0.5% Nafion in a 2-propanol solution was cast on top of the catalyst layer. Three replicates were prepared for each sample. After that, the electrode was used for cyclic voltammetry experiments in a 3-electrode cell, using a platinum gauze as a counter-electrode and Ag | AgCl | KCl^{sat} as a reference electrode. The electrolyte (0.5 M H_2SO_4, pH 0.3) was purged with nitrogen for 30 min prior to the experiments. The electrode was first scanned for 8 cycles between −0.2 V and 1.2 V vs. Ag | AgCl | KCl^{sat}; after that, the solution was saturated with pure CO by bubbling for 30 min. Then, a potential of 0 V vs. Ag | AgCl | KCl^{sat} was applied for 30 min. Then, still applying the potential, the solution was purged with N_2 for 30 min and then the potential was scanned between 0 V and 1.2 V vs. Ag | AgCl | KCl^{sat} for three scans. The first scan showed an oxidation peak around 0.7 V vs. Ag | AgCl | KCl^{sat}, corresponding to the oxidation of chemisorbed CO. The area was determined by integrating the charge of the peak and dividing by the CO charge for cm^2 (0.420 mC/cm^2, for linearly bond CO) and then dividing by the metal loading.

3.3. Catalytic Tests

Aqueous phase reforming of ethylene glycol was carried out in a 100 mL stainless steel autoclave equipped with a mechanical stirrer and a temperature controller. The catalyst (equivalent to 5.1 μmol Pt) and 20 mL of a 5 wt.% aqueous EG solution were loaded into the vessel. The reactor was thoroughly purged with nitrogen and pressurized to an initial pressure of 10 bar, which served as an internal standard for the final quantification of the products present in the gas phase. The mixture was subsequently stirred at 1000 rpm and heated to 220 °C. Heating time was approximately 10 min. After 4 h at 220 °C, the reactor was quenched to room temperature in an ice water bath. Gaseous products were collected in a multilayer foil gas sampling bag (Supelco, Bellefonte, PA, USA). After depressurization, the liquid products were collected and filtered. The spent catalyst was recovered by filtration, washed with a copious amount of DI water, and dried overnight at 100 °C. Similar procedures were performed at 240 °C, 7 bar of N_2, and for 2 h.

Gas and liquid phase products were analyzed by gas chromatography (Shimadzu 2010Pro; Shimadzu, Kyoto, Japan) equipped with a thermal conductivity detector (TCD) and a flame ionization detector (FID). H_2, CO, CO_2, N_2, and CH_4 were detected by TCD using a Carboxen 1010 (Supelco, Bellefonte, PA, USA). Nitrogen was used as an internal standard for the quantification of permanent gasses and methane. Volatile liquid phase products (methanol, ethanol, acetic acid, unreacted ethylene glycol) were also analyzed by gas chromatography equipped with a CP-Wax 52 CB GC column (Agilent, Santa Clara, CA, USA) and a flame ionization detector (FID). The quantification of the products was performed with a calibration curve using 1-propanol as an internal standard.

Recycling tests were performed as follows: 200 mg of a catalyst was loaded into the reactor and the reaction was performed at 240 °C for 2 h. After the catalyst was filtered, and washed with a copious amount of DI water, it was dried in an oven at 105 °C overnight. Then, the resulting solid was loaded back into an autoclave to perform the next cycle. Gas and liquid products were analyzed as previously mentioned. The procedure was repeated 4 times. Loss of the catalyst during handling was taken into account in the next cycle.

Aqueous phase reforming of PET was performed in a 100 mL stainless steel autoclave equipped with a mechanical stirrer and a temperature controller. Typically, 100 mg of a catalyst was charged with 700 mg of crushed PET and 20 mL of water in the reactor. The reactor was purged with N_2 several times and charged with 7 bar of N_2, followed by heating up to 240 °C within 15 min. After 4 h, the reactor was cooled with an ice bath. Gas was collected with a gas bag and the solid was separated by filtration. The gas phase and liquid phase products were analyzed by GC-FID. The solid phase was washed with concentrated NaOH to dissolve terephthalic acid (TPA), followed by neutralization to recover TPA crystals.

4. Conclusions

To summarize, Pt NPs of different size distributions (mean diameter below 2 nm) were deposited on commercially available carbons (i.e., Vulcan XC72, C^V, and/or Ketjenblack EC-600JD, C^K) following different synthesis protocols by the metal vapor synthesis method. Their catalytic efficiency was evaluated and compared for the aqueous phase reforming of ethylene glycol. The most active and stable catalyst, Pt_A/C^K, displayed a mean Pt NP size of 1.5 nm, was obtained from Pt–acetone, and was highly dispersed on the carbon support with the highest surface area (i.e., C^K). The system exhibits very high H_2 site time yield (8.92 min^{-1} at 220 °C) compared to a commercially available alumina-supported Pt catalyst. High stability towards metal sintering was proven for both high-temperature treatment (i.e., 500 °C) and several batch recycling runs under the reaction conditions (240 °C) with negligible H_2 yield loss and/or metal leaching. In contrast, an analogous system supported on the same carbon but containing a major fraction of sub-nanometer Pt single atoms and clusters showed an inferior catalytic efficiency together with a low stability towards the formation of large particles (>3 nm). Our study suggests an optimal Pt particle size of around 1.5 nm for this process as a good compromise between Pt dispersion and stability.

The MVS-derived catalyst was also effectively applied to the APR process of polyethylene terephthalate (PET), showing potential for H_2 production from recycled plastics. This work highlights the fundamental role of the use of advanced synthesis approaches that are able to strictly control metal nanoparticle size and the kind of support materials in optimizing APR processes for sustainable hydrogen production.

Supplementary Materials: The following supporting information can be downloaded at: https://www.mdpi.com/article/10.3390/catal14110798/s1, Section S1: Parameter for Evaluation of APR process; Table S1. Morphological properties of CV and CK; Figure S1. Representative TEM image at high magnification (bar in images corresponds to 10 nm) of PtM/CK; Figure S2. Representative HAADF-ac-STEM images of PtM/CK-HT; Figure S3: Blank voltammetry (8th scan) of the various Pt/C samples; Figure S4. EG conversion and hydrogen productivity of PtA/CK and commercial Pt/Al2O3; Figure S5. Representative TEM images and Pt particle size distribution of commercial Pt/Al2O3 1 wt.%; Figure S6. Representative TEM image and Pt particle size distribution of PtA/CK after 4 catalytic runs; Table S2. Gas composition of APR of PET with Pt-based catalyst.

Author Contributions: Conceptualization, X.T.N. and C.E.; methodology, X.T.N. and C.E.; validation, X.T.N., E.P. and C.E.; formal analysis, X.T.N., E.K. and J.F.; data curation, X.T.N., E.K. and C.E.; writing—original draft preparation, X.T.N.; writing—review and editing, X.T.N., E.K., T.S., E.P., J.F., W.O. and C.E.; visualization, X.T.N., E.K. and C.E.; supervision, T.S. and C.E.; project administration, C.E.; funding acquisition, C.E. All authors have read and agreed to the published version of the manuscript.

Funding: This research was funded by the European Union—NextGeneration EU through the Italian Ministry of Environment and Energy Security POR H_2 AdP MMES/ENEA with involvement of CNR and RSE, PNRR—Mission 2, Component 2, Investment 3.5 "Ricerca e sviluppo sull'idrogeno", CUP: B93C22000630006. XT.N. and C. E. would also like to thank the European Union's Horizon 2020 Research and Innovation Program under the Marie Skłodowska-Curie Actions−Innovative Training Networks (MSCA-ITN) BIKE project, Grant Agreement 813748.

Data Availability Statement: All data generated or analyzed during this study are included in this published article and its Supplementary Information Files.

Acknowledgments: The authors thank Mohsen Danaie from ePSIC, Diamond Light Source, Harwell Science & Innovation Campus, UK, for his contribution to HAADF STEM images. We also thank Carlo Bartoli from ICCOM-CNR—Florence for his assistance in the catalytic experiment. We also thank Diamond Light Source for access and support in use of the electron Physical Science Imaging Centre (Instrument E01 and proposal number MG33438) that contributed to the results presented here. We would like to thank the ERDF (European Regional Development Fund) and Wolfson Foundation for funding the CCI (Cardiff Catalysis Institute) Electron Microscopy Facility.

Conflicts of Interest: The authors declare no conflicts of interest.

References

1. Dunn, S. Hydrogen Futures: Toward a Sustainable Energy System. *Int. J. Hydrogen Energy* **2002**, *27*, 235–264. [CrossRef]
2. Cortright, R.D.; Davda, R.R.; Dumesic, J.A. Hydrogen from Catalytic Reforming of Biomass-Derived Hydrocarbons in Liquid Water. *Nature* **2002**, *418*, 964–967. [CrossRef] [PubMed]
3. González-Arias, J.; Zhang, Z.; Reina, T.R.; Odriozola, J.A. Hydrogen Production by Catalytic Aqueous-Phase Reforming of Waste Biomass: A Review. *Environ. Chem. Lett.* **2023**, *21*, 3089–3104. [CrossRef]
4. Geyer, R.; Jambeck, J.R.; Law, K.L. Production, Use, and Fate of All Plastics Ever Made. *Sci. Adv.* **2017**, *3*, e1700782. [CrossRef]
5. Ruiz-Garcia, C.; Baeza, J.A.; Oliveira, A.S.; Roldán, S.; Calvo, L.; Gilarranz, M.A. Exploration of Operating Conditions in the Direct Aqueous-Phase Reforming of Plastics. *Fuel* **2024**, *374*, 132446. [CrossRef]
6. Davda, R.R.; Shabaker, J.W.; Huber, G.W.; Cortright, R.D.; Dumesic, J.A. A Review of Catalytic Issues and Process Conditions for Renewable Hydrogen and Alkanes by Aqueous-Phase Reforming of Oxygenated Hydrocarbons over Supported Metal Catalysts. *Appl. Catal. B Environ.* **2005**, *56*, 171–186. [CrossRef]
7. Chen, G.; Li, W.; Chen, H.; Yan, B. Progress in the Aqueous-Phase Reforming of Different Biomass-Derived Alcohols for Hydrogen Production. *J. Zhejiang Univ.-Sci. A* **2015**, *16*, 491–506. [CrossRef]
8. Pipitone, G.; Zoppi, G.; Pirone, R.; Bensaid, S. A Critical Review on Catalyst Design for Aqueous Phase Reforming. *Int. J. Hydrogen Energy* **2022**, *47*, 151–180. [CrossRef]
9. Davda, R.R.; Shabaker, J.W.; Huber, G.W.; Cortright, R.D.; Dumesic, J.A. Aqueous-Phase Reforming of Ethylene Glycol on Silica-Supported Metal Catalysts. *Appl. Catal. B Environ.* **2003**, *43*, 13–26. [CrossRef]

10. Huber, G.W.; Shabaker, J.W.; Evans, S.T.; Dumesic, J.A. Aqueous-Phase Reforming of Ethylene Glycol over Supported Pt and Pd Bimetallic Catalysts. *Appl. Catal. B Environ.* **2006**, *62*, 226–235. [CrossRef]
11. Boudart, M. Catalysis by Supported Metals**This Work Was Sponsored by Grant GK 648 of the National Science Foundation. Its Continuity over the Years Has Been Assured by a Generous Grant from the Petroleum Research Fund of the American Chemical Society. In *Advances in Catalysis*; Eley, D.D., Pines, H., Weisz, P.B., Eds.; Academic Press: Cambridge, MA, USA, 1969; Volume 20, pp. 153–166. ISBN 0360-0564.
12. Lehnert, K.; Claus, P. Influence of Pt Particle Size and Support Type on the Aqueous-Phase Reforming of Glycerol. *Catal. Commun.* **2008**, *9*, 2543–2546. [CrossRef]
13. Wawrzetz, A.; Peng, B.; Hrabar, A.; Jentys, A.; Lemonidou, A.A.; Lercher, J.A. Towards Understanding the Bifunctional Hydrodeoxygenation and Aqueous Phase Reforming of Glycerol. *J. Catal.* **2010**, *269*, 411–420. [CrossRef]
14. Barbelli, M.L.; Pompeo, F.; Santori, G.F.; Nichio, N.N. Pt Catalyst Supported on α-Al_2O_3 Modified with CeO_2 and ZrO_2 for Aqueous-Phase-Reforming of Glycerol. *Catal. Today* **2013**, *213*, 58–64. [CrossRef]
15. Kim, Y.; Kim, M.; Jeong, H.; Kim, Y.; Choi, S.H.; Ham, H.C.; Lee, S.W.; Kim, J.Y.; Song, K.H.; Yoon, C.W.; et al. High Purity Hydrogen Production via Aqueous Phase Reforming of Xylose over Small Pt Nanoparticles on a γ-Al_2O_3 Support. *Int. J. Hydrogen Energy* **2020**, *45*, 13848–13861. [CrossRef]
16. Chen, A.; Chen, P.; Cao, D.; Lou, H. Aqueous-Phase Reforming of the Low-Boiling Fraction of Bio-Oil for Hydrogen Production: The Size Effect of Pt/Al_2O_3. *Int. J. Hydrogen Energy* **2015**, *40*, 14798–14805. [CrossRef]
17. Yamaguchi, W.; Tai, Y. Size-Dependent Catalytic Activity of Platinum Nanoparticles for Aqueous-Phase Reforming of Glycerol. *Chem. Lett.* **2014**, *43*, 313–315. [CrossRef]
18. Cui, X.; Li, W.; Ryabchuk, P.; Junge, K.; Beller, M. Bridging Homogeneous and Heterogeneous Catalysis by Heterogeneous Single-Metal-Site Catalysts. *Nat. Catal.* **2018**, *1*, 385–397. [CrossRef]
19. Li, Z.; Ji, S.; Liu, Y.; Cao, X.; Tian, S.; Chen, Y.; Niu, Z.; Li, Y. Well-Defined Materials for Heterogeneous Catalysis: From Nanoparticles to Isolated Single-Atom Sites. *Chem. Rev.* **2020**, *120*, 623–682. [CrossRef]
20. Shabaker, J.W.; Davda, R.R.; Huber, G.W.; Cortright, R.D.; Dumesic, J.A. Aqueous-Phase Reforming of Methanol and Ethylene Glycol over Alumina-Supported Platinum Catalysts. *J. Catal.* **2003**, *215*, 344–352. [CrossRef]
21. Koichumanova, K.; Vikla, A.K.K.; de Vlieger, D.J.M.; Seshan, K.; Mojet, B.L.; Lefferts, L. Towards Stable Catalysts for Aqueous Phase Conversion of Ethylene Glycol for Renewable Hydrogen. *ChemSusChem* **2013**, *6*, 1717–1723. [CrossRef]
22. Antal, M.J., Jr.; Allen, S.G.; Schulman, D.; Xu, X.; Divilio, R.J. Biomass Gasification in Supercritical Water. *Ind. Eng. Chem. Res.* **2000**, *39*, 4040–4053. [CrossRef]
23. Vikla, A.K.K.; Simakova, I.; Demidova, Y.; Keim, E.G.; Calvo, L.; Gilarranz, M.A.; He, S.; Seshan, K. Tuning Pt Characteristics on Pt/C Catalyst for Aqueous-Phase Reforming of Biomass-Derived Oxygenates to Bio-H_2. *Appl. Catal. A Gen.* **2021**, *610*, 117963. [CrossRef]
24. Pitzalis, E.; Psaro, R.; Evangelisti, C. From Metal Vapor to Supported Single Atoms, Clusters and Nanoparticles: Recent Advances to Heterogeneous Catalysts. *Inorganica Chim. Acta* **2022**, *533*, 120782. [CrossRef]
25. Oberhauser, W.; Evangelisti, C.; Tiozzo, C.; Bartoli, M.; Frediani, M.; Passaglia, E.; Rosi, L. Platinum Nanoparticles onto Pegylated Poly(Lactic Acid) Stereocomplex for Highly Selective Hydrogenation of Aromatic Nitrocompounds to Anilines. *Appl. Catal. A Gen.* **2017**, *537*, 50–58. [CrossRef]
26. Oberhauser, W.; Evangelisti, C.; Jumde, R.P.; Psaro, R.; Vizza, F.; Bevilacqua, M.; Filippi, J.; Machado, B.F.; Serp, P. Platinum on Carbonaceous Supports for Glycerol Hydrogenolysis: Support Effect. *J. Catal.* **2015**, *325*, 111–117. [CrossRef]
27. Oberhauser, W.; Evangelisti, C.; Tiozzo, C.; Vizza, F.; Psaro, R. Lactic Acid from Glycerol by Ethylene-Stabilized Platinum-Nanoparticles. *ACS Catal.* **2016**, *6*, 1671–1674. [CrossRef]
28. Borodziński, A.; Bonarowska, M. Relation between Crystallite Size and Dispersion on Supported Metal Catalysts. *Langmuir* **1997**, *13*, 5613–5620. [CrossRef]
29. Klabunde, K.J.; Li, Y.X.; Tan, B.J. Solvated Metal Atom Dispersed Catalysts. *Chem. Mater.* **1991**, *3*, 30–39. [CrossRef]
30. Al-Shareef, R.; Harb, M.; Saih, Y.; Ould-Chikh, S.; Anjum, D.H.; Candy, J.-P.; Basset, J.-M. Precise Control of Pt Particle Size for Surface Structure–Reaction Activity Relationship. *J. Phys. Chem. C* **2018**, *122*, 23451–23459. [CrossRef]
31. Chen, J.; Chan, K.-Y. Size-Dependent Mobility of Platinum Cluster on a Graphite Surface. *Mol. Simul.* **2005**, *31*, 527–533. [CrossRef]
32. Martin, T.E.; Mitchell, R.W.; Boyes, E.D.; Gai, P.L. Atom-by-Atom Analysis of Sintering Dynamics and Stability of Pt Nanoparticle Catalysts in Chemical Reactions. *Philos. Trans. R. Soc. A Math. Phys. Eng. Sci.* **2020**, *378*, 20190597. [CrossRef] [PubMed]
33. Maillard, F.; Savinova, E.R.; Simonov, P.A.; Zaikovskii, V.I.; Stimming, U. Infrared Spectroscopic Study of CO Adsorption and Electro-Oxidation on Carbon-Supported Pt Nanoparticles: Interparticle versus Intraparticle Heterogeneity. *J. Phys. Chem. B* **2004**, *108*, 17893–17904. [CrossRef]
34. Maillard, F.; Schreier, S.; Hanzlik, M.; Savinova, E.R.; Weinkauf, S.; Stimming, U. Influence of Particle Agglomeration on the Catalytic Activity of Carbon-Supported Pt Nanoparticles in CO Monolayer Oxidation. *Phys. Chem. Chem. Phys.* **2005**, *7*, 385–393. [CrossRef]
35. Ciapina, E.G.; Santos, S.F.; Gonzalez, E.R. Electrochemical CO Stripping on Nanosized Pt Surfaces in Acid Media: A Review on the Issue of Peak Multiplicity. *J. Electroanal. Chem.* **2018**, *815*, 47–60. [CrossRef]
36. Shabaker, J.W.; Dumesic, J.A. Kinetics of Aqueous-Phase Reforming of Oxygenated Hydrocarbons: Pt/Al_2O_3 and Sn-Modified Ni Catalysts. *Ind. Eng. Chem. Res.* **2004**, *43*, 3105–3112. [CrossRef]

37. Amin, A.S.; Caidi, A.; Lange, T.; Radev, I.; Sandbeck, D.J.S.; Philippi, W.; Kräenbring, M.-A.; Öztürk, M.; Peinecke, V.; Lerche, D.; et al. Key Control Characteristics of Carbon Black Materials for Fuel Cells and Batteries for a Standardized Characterization of Surface Properties. *Part. Part. Syst. Charact.* **2024**, 2400069. [CrossRef]
38. Bevilacqua, M.; Bianchini, C.; Marchionni, A.; Filippi, J.; Lavacchi, A.; Miller, H.; Oberhauser, W.; Vizza, F.; Granozzi, G.; Artiglia, L.; et al. Improvement in the Efficiency of an OrganoMetallic Fuel Cell by Tuning the Molecular Architecture of the Anode Electrocatalyst and the Nature of the Carbon Support. *Energy Environ. Sci.* **2012**, *5*, 8608–8620. [CrossRef]
39. Yang, Z.; Kim, C.; Hirata, S.; Fujigaya, T.; Nakashima, N. Facile Enhancement in CO-Tolerance of a Polymer-Coated Pt Electrocatalyst Supported on Carbon Black: Comparison between Vulcan and Ketjenblack. *ACS Appl. Mater. Interfaces* **2015**, *7*, 15885–15891. [CrossRef]
40. Kandoi, S.; Greeley, J.; Simonetti, D.; Shabaker, J.; Dumesic, J.A.; Mavrikakis, M. Reaction Kinetics of Ethylene Glycol Reforming over Platinum in the Vapor versus Aqueous Phases. *J. Phys. Chem. C* **2011**, *115*, 961–971. [CrossRef]
41. Faheem, M.; Saleheen, M.; Lu, J.; Heyden, A. Ethylene Glycol Reforming on Pt(111): First-Principles Microkinetic Modeling in Vapor and Aqueous Phases. *Catal. Sci. Technol.* **2016**, *6*, 8242–8256. [CrossRef]
42. Gu, G.H.; Wittreich, G.R.; Vlachos, D.G. Microkinetic Modeling of Aqueous Phase Biomass Conversion: Application to Ethylene Glycol Reforming. *Chem. Eng. Sci.* **2019**, *197*, 415–418. [CrossRef]
43. George, N.; Kurian, T. Recent Developments in the Chemical Recycling of Postconsumer Poly(Ethylene Terephthalate) Waste. *Ind. Eng. Chem. Res.* **2014**, *53*, 14185–14198. [CrossRef]
44. Su, H.; Li, T.; Wang, S.; Zhu, L.; Hu, Y. Low-Temperature Upcycling of PET Waste into High-Purity H_2 Fuel in a One-Pot Hydrothermal System with in Situ CO_2 Capture. *J. Hazard. Mater.* **2023**, *443*, 130120. [CrossRef] [PubMed]
45. Su, H.; Hu, Y.; Feng, H.; Zhu, L.; Wang, S. Efficient H_2 Production from PET Plastic Wastes over Mesoporous Carbon-Supported Ru-ZnO Catalysts in a Mild Pure-Water System. *ACS Sustain. Chem. Eng.* **2023**, *11*, 578–586. [CrossRef]
46. Horányi, G.; Nagy, F. Investigation of Adsorption Phenomena on Platinized Platinum Electrodes by Tracer Methods: IV. Adsorption of Aromatic Compounds. *J. Electroanal. Chem. Interfacial Electrochem.* **1971**, *32*, 275–282. [CrossRef]
47. Wu, Y.; Cai, S.; Wang, D.; He, W.; Li, Y. Syntheses of Water-Soluble Octahedral, Truncated Octahedral, and Cubic Pt–Ni Nanocrystals and Their Structure–Activity Study in Model Hydrogenation Reactions. *J. Am. Chem. Soc.* **2012**, *134*, 8975–8981. [CrossRef]
48. Shiraishi, Y.; Tanaka, H.; Sakamoto, H.; Hayashi, N.; Kofuji, Y.; Ichikawa, S.; Hirai, T. Synthesis of Au Nanoparticles with Benzoic Acid as Reductant and Surface Stabilizer Promoted Solely by UV Light. *Langmuir* **2017**, *33*, 13797–13804. [CrossRef]